Analog of a Quantum Heat Engine Using a Single-Spin Qubit

K. Ono,[1,2,*] S. N. Shevchenko[ID],[3,4,5,†] T. Mori,[6] S. Moriyama[ID],[7] and Franco Nori[ID][5,8,‡]

[1]*Advanced Device Laboratory, RIKEN, Wako-shi, Saitama 351-0198, Japan*
[2]*CEMS, RIKEN, Wako-shi, Saitama 351-0198, Japan*
[3]*B. Verkin Institute for Low Temperature Physics and Engineering, Kharkov 61103, Ukraine*
[4]*V. N. Karazin Kharkiv National University, Kharkov 61022, Ukraine*
[5]*Theoretical Quantum Physics Laboratory, Cluster for Pioneering Research, RIKEN, Wako-shi, Saitama 351-0198, Japan*
[6]*Device Technology Research Institute (D-Tech), National Institute of Advanced Industrial Science and Technology (AIST), Tsukuba, Ibaraki 305-8568, Japan*
[7]*Department of Electrical and Electronic Engineering, Tokyo Denki University, Adachi-ku, Tokyo 120-8551, Japan*
[8]*Department of Physics, The University of Michigan, Ann Arbor, Michigan 48109-1040, USA*

A quantum two-level system with periodically modulated energy splitting could provide a minimal universal quantum heat machine. We present the experimental realization and the theoretical description of such a two-level system as an impurity electron spin in a silicon tunnel field-effect transistor. In the incoherent regime, the system can behave analogously to either an Otto heat engine or a refrigerator. The coherent regime could be described as a superposition of those two regimes, producing specific interference fringes in the observed source-drain current.

Introduction.—Thermodynamics was originally developed for classical many-particle systems, but recently it is being applied to the description of individual quantum systems. This emergent field is known as quantum thermodynamics [1]. In several review articles, different types of quantum heat engines were considered, e.g., Refs. [2–6].

What essentially distinguishes a working medium of a quantum heat engine from a classical one is the ability to be in a coherent superposition of its states [7,8]. In this way, the study of superpositional interference phenomena in prototypical quantum heat engines is important since this can provide a quantum advantage in their performance; that is, the ability of a quantum heat engine to produce more power than an equivalent classical heat engine [8,9].

The simplest realization of a quantum heat machine would be a two-level system. Such a system, with a periodically modulated energy splitting, could work as either a heat engine or a refrigerator, thus providing a minimal universal quantum heat machine [10–12]. Different proposed realizations are based on either natural or artificial atoms [13], including superconducting and semiconducting circuits, e.g., Refs. [14–22]. Recently, experimental realizations of single-atom heat engines were demonstrated with trapped ions [23–25] and nitrogen-vacancy centers in diamond [8]. In this Letter, we present an experimental realization and a theoretical description of heat-engine-like cycles for highly controllable spin-1/2 states.

A heat machine can have two possible regimes, corresponding to the engine-type and refrigerator-type cycles, as shown on the left in Fig. 1. The right panels of Fig. 1 show the realizations of these two regimes using a two-level system with modulated energy levels. Consider first the situation when the period of the drive $2\pi/\Omega$ is much larger
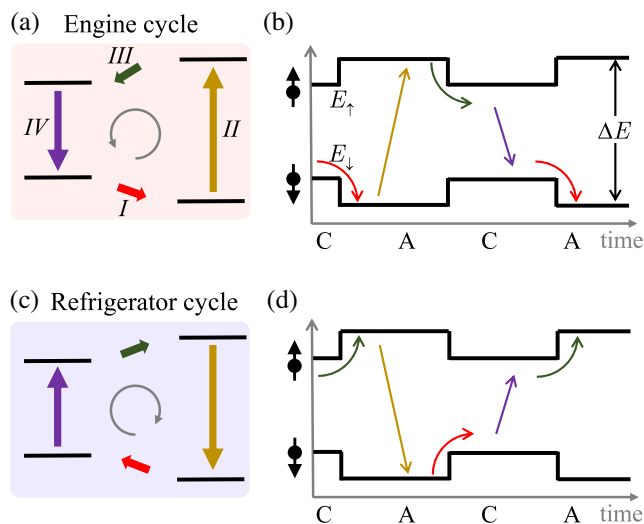

FIG. 1. Interpretation of the modulated dynamics in terms of a heat engine or a refrigerator. The heat-engine-like cycle shown in (a) can be realized by modulating the energy levels as shown in (b). The energy-level gap ΔE varies between larger "A" and smaller "C" values. The arrows show the incoherent dynamics with resonant excitation during the large-energy-gap stage "A." Panels (c) and (d) present the incoherent dynamics with resonant excitation during the small-energy-gap stage, which is reminiscent of the refrigerator cycle.

than the decoherence time T_2, which we denote as the *incoherent* regime. Figure 1(b) corresponds to the situation in which the resonant driving increases the upper-level occupation during the large-energy-gap stage ["A" in Fig. 1(b)], followed by a relaxation to the ground state ["C" in Fig. 1(b)]. This is analogous to the heat-engine cycle in Fig. 1(a). For another choice of parameters, Fig. 1(d) illustrates the situation in which the resonant driving increases the upper-level occupation during the small-energy-gap stage "C" with the relaxation during stage "A." This is analogous to the refrigerator cycle in Fig. 1(c).

Note the similarity between our heat-engine-like cycles and the so-called Sisyphus lasing and cooling cycles, which also describe the periodic evolution of a modulated dissipative two-level system studied in Refs. [26–30]. These processes take place when the period of the energy-level modulation is comparable to the relaxation time. Then the cycle has four stages: the resonant excitation into the upper state, the adiabatic evolution within this state, the relaxation to the ground state, and the adiabatic evolution again.

When decreasing the ratio of the driving period $2\pi/\Omega$ to the decoherence time T_2, we expect that the coherence will result in interference between the wave-function components [31–34]. This regime, when $T_2 \gtrsim 2\pi/\Omega$, can be denoted as a *coherent* regime. In this Letter, we study both the incoherent quantum "heat" cycles, like in Fig. 1, and coherent dynamics that result in interference fringes. We study a two-level system with modulated energy levels being driven by a periodic frequency-modulated signal, which makes the device highly controllable by several parameters (including the frequency and the amplitude of modulations). We present an experimental realization and a theoretical description of such a system, realized as an electron spin of an impurity placed in a silicon tunnel field-effect transistor (TFET). Such a system allows versatile control via the microwave driving and the modulation of the Landé g factor. Note that almost all works on quantum heat engines have been theoretical. Our device has the potential to realize these experimentally.

Device.—Our spin-qubit device is based on a short-channel TFET. Deep impurities are intensively ion implanted to the channel of the TFET. At room temperature, they act as quantum dots [35]. For a device with a channel length of ∼80 nm, under a source voltage V_S and a gate voltage V_G, the source-to-drain conduction is dominated by tunneling through two impurities, i.e., one deep impurity and a shallow impurity located near the deep impurity. For more details, see the Supplemental Material [36].

This double-dot-like transport exhibits spin-blockade phenomena [37–40] and enables the time-ensemble measure of an electron spin of one of the impurities. We focused on the small source-drain current under the spin blockade condition. Under appropriate dc and ac magnetic fields, the source-drain current increases due to the lifting of the spin blockade by the electron spin resonance (ESR) of one of the impurities [41]. Thus, sweeping the frequency of the ac component of the magnetic field, for a fixed dc magnetic field the source-drain current shows a peak at the ESR frequency, and the peak's height is proportional to the excitation probability of the spin qubit.

We measure the spin-blockade source-drain current of the device at 1.6 K with dc magnetic field $B \approx 0.28$ T and ac magnetic field with microwave (MW) frequency ∼9 GHz. An observed linewidth of ∼4 MHz, as well as a Rabi oscillation measurement [35], show a coherence time of 0.25 μs. This timescale includes the effect of finite lifetime of the spin on the impurity. This finite lifetime is due to the finite mean-stay time of the electron on the impurity in the tunneling transport through the impurities. Thus, the spin on the impurity is replaced at this timescale. Theoretically, this situation is described by introducing the phenomenological relaxation and decoherence times $T_{1,2}$. For a two-level system, T_1 describes the relaxation from the excited state, while T_2 describes the lifetime of the coherence in the system.

Qubit energy modulation.—We found that the g factor of one of the impurities can be tuned by the gate voltage V_G. This is due to the Stark effect [42]. In our device, ∼1% of the g factor can be tuned by changing V_G within ± 20 mV. Note that the spin-blockade condition is still kept in our device if we change V_G by such amount. The fast modulation of V_G, and thus the energy of the spin qubit, is carried out by adding the radio frequency modulation to the gate electrode. Square waves with frequencies from 0.05 to 10 MHz are used. See Refs. [35,42] for further details on the device, spin-qubit measure, and V_G modulation, and see Refs. [9,43,44] for the study of other modulation pulses, the ones realizing the counterdiabatic driving in particular.

MW frequency modulation.—We use the frequency modulation (FM) function of our MW generator, where the FM is proportional to the voltage signal fed to the external input. The two-channel arbitrary waveform generator was used for the V_G modulation, and the voltage was used for microwave frequency modulation. It is important to note that the bandwidth of the arbitrary waveform generator is ∼100 MHz, so this modulation never excites higher-lying spin states, including the $1/2$ spin of another impurity whose ESR frequency is 1 GHz higher than the focused spin. Thus, changes of both the qubit energy and MW frequency can be regarded as adiabatic. For the synchronized modulation of both the qubit energy and the MW frequency, we used two square-wave signals with tunable amplitudes and phase differences, feeding one signal to the gate electrode and another one to the input for the FM signal on the MW generator.

Theoretical description.—We describe this spin-qubit device as a driven two-level system, which is amplitude and

frequency modulated, with the pseudospin Hamiltonian $H(t) = B_z(t)\sigma_z/2 + B_x(t)\sigma_x/2$. In other words, we consider a single 1/2-spin subject to a fast microwave driving and a slow rf modulation of both amplitude *and* frequency. Note that in our previous work [42] we only considered amplitude modulation.

The longitudinal part of the Hamiltonian $H(t)$ is defined by the Zeeman splitting $B_z(t) = g(t)\mu_B B$. The time-dependent gate voltage changes the g factor by a small value [45], and we have $B_z/\hbar = \omega_q + \delta\omega_q s(t)$, with $\delta\omega_q \ll \omega_q$, where $\omega_q = 2\pi f_q$ represents the ESR frequency, and $\delta\omega_q$ describes the *amplitude modulation*. In this Letter, we consider a square-wave modulation $s(t) = \mathrm{sgn}[\cos\Omega t]$. The transverse part of the Hamiltonian is defined by the frequency-modulated MW voltage applied to the substrate $B_x/\hbar = 2G\cos[\omega_{FM}(t)t]$ with a frequency $\omega_{FM}(t) = \omega_{MW} + \delta\omega_{MW}s_\phi(t)$, which is modulated by the phase-shifted signal $s_\phi(t) = \mathrm{sgn}[\cos(\Omega t + \phi)]$. Here G stands for the amplitude, which is defined by the microwave power at the microwave-generator output, and $\omega_{MW} = 2\pi f_{MW}$ is the microwave circular frequency. The modulation is assumed to be slow, i.e., $\Omega \ll \omega_{MW}$, and with a small amplitude, $\delta\omega_{MW} \ll \omega_{MW}$, where $\delta\omega_{MW}$ describes the *frequency modulation*. (About amplitude and frequency modulation, see also Refs. [46–51].) With the Hamiltonian $H(t)$, we solve the Bloch equations, as described in detail in the Supplemental Material [36] (see also Refs. [52,53]). Analytical stationary solutions of the Bloch equations allow us to obtain the upper-level occupation probability P_+, as shown in the lower part of Fig. 3, while the numerical solution gives the time-dependent occupation $P_+(t)$ [36].

The modulated qubit energy levels $E_{\uparrow,\downarrow} = \pm\frac{1}{2}\Delta E = \pm(\hbar/2)[\omega_q + \delta\omega_q s(t)]$ are plotted as a function of the dimensionless time $\tau = \Omega t/2\pi$ in the upper panel in Fig. 2(a). The lower panel of Fig. 2(a) presents the time dependence of the modulated microwave frequency $\omega_{FM}(t)$. This frequency is phase shifted with respect to the energy-level modulation.

The qubit experiences a resonant excitation when $\Delta E(t) = \hbar\omega_{FM}(t)$. This relation, written as $\omega_q + \delta\omega_q s(t) = \omega_{MW} + \delta\omega_{MW}s_\phi(t)$, allows four possibilities for the resonant excitation: $\Delta\omega \equiv \omega_q - \omega_{MW} = \Delta\omega^{(A,B,C,D)}$, where $\Delta\omega^{(A,B)} = -\delta\omega_q \pm \delta\omega_{MW}$ and $\Delta\omega^{(C,D)} = \delta\omega_q \mp \delta\omega_{MW}$. This means that, if one of the conditions is met, $\Delta\omega = \Delta\omega^{(i)}$, then during the ith stage the resonant condition is fulfilled.

Note that the above conditions are valid for relatively small modulation frequencies when the respective period is much larger than the decoherence time $2\pi/\Omega \gg T_2$. In this case, the incoherent dynamics during one of the stages does not influence the dynamics of the later stages. And indeed, in the source-drain current the four resonance
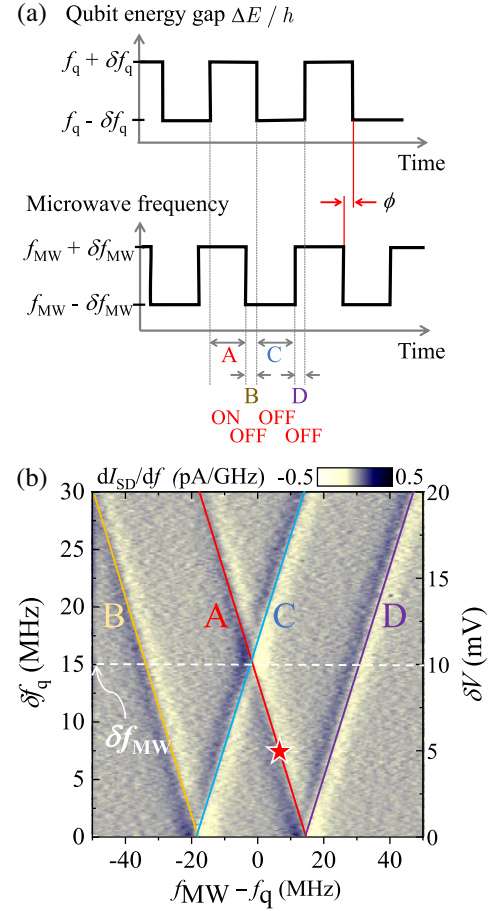

(a) Qubit energy gap $\Delta E / h$

Microwave frequency

(b) dI_{SD}/df (pA/GHz)

FIG. 2. Amplitude- and frequency-modulated two-level system. In the upper panel of (a), the qubit energy $\Delta E(t) = E_\uparrow - E_\downarrow = h[f_q + \delta f_q s(t)]$ is shown to be modulated in amplitude; in the lower panel, the modulated driving (microwave) frequency $f_{FM}(t) = f_{MW} + \delta f_{MW}s_\phi(t)$ is presented. The phase shift ϕ corresponds to four stages of evolution, denoted from "A" to "D." We show the situation when the qubit is resonantly excited during stage "A", as in Fig. 1(b). Then the coupling between the drive and the qubit is "ON" during this stage and "OFF" during the other stages. The four possible resonant excitations are shown by the inclined lines in (b), where the colors correspond to the four stages in (a). Panel (b) presents the derivative of the source-drain current as a function of the frequency detuning and the amplitude of the energy-level modulation at $\delta f_{MW} = 15$ MHz.

conditions were observed as the inclined lines along $\Delta\omega = \Delta\omega^{(A...D)}$ [Fig. 2(b)].

Specifically, we show schematically the resonant excitation in Fig. 2(a) and Fig. 1(b) for the situation when the resonant condition is for stage "A," where $\Delta\omega = \Delta\omega^{(A)}$. In Fig. 1(b), we start from the system in the ground state. Then the qubit becomes partially excited, and later on we have full relaxation back to the ground state. This is shown for the incoherent regime. In the coherent regime, the relaxation time of the population is longer than the driving period (so that $T_2 \gtrsim 2\pi/\Omega$), and the interference between
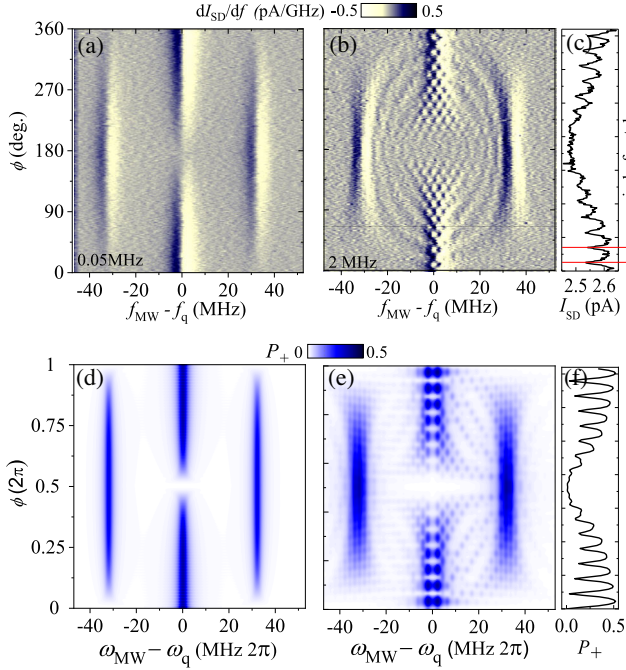
FIG. 3. Incoherent and coherent regimes at $\delta f_{MW} = \delta f_q$. Source-drain current I_{SD} as a function of the frequency detuning $(f_{MW} - f_q)$ and the phase difference ϕ, in the incoherent (a) and coherent (b) regimes, for the modulation frequencies $\Omega/2\pi = 0.05$ and 2 MHz, respectively. (c) is the cross section of (b) along the line $f_{MW} = f_q$. (d)–(f) show the theoretically computed respective upper-level occupation probability. Note the small "notches" in (b),(c) and (e),(f).

different stages takes place, which we will consider later in more detail.

Analogy to a heat engine.—First, it is possible to introduce an (effective) temperature T as the value defining the energy-level populations P_+ and $P_- = 1 - P_+$ with the relation $(P_-/P_+) = \exp[(\Delta E/k_B T)]$ [54,55]. Then the driven and relaxed stages, with P_+ close to 1/2 and 0, respectively, determine the cold and hot reservoir temperatures [25]. The emulation of a quantum heat engine is then completed by associating the energy-level distance ΔE with the volume of a working gas in the corresponding macroscopic engine [25,54]. With these, we are prepared to describe the driven evolution of our single-spin quantum machine.

We now consider, for simplicity, $\phi = 0$, while a nonzero phase shift ϕ gives an additional degree of control. Then stages "D" and "B" in Fig. 2(a) collapse, and we have the alternation of stages "A" and "C" only, as in Fig. 1. We start in Fig. 1(a),(b) with $\Delta\omega = \Delta\omega^{(A)}$. Then the changes in the energy-level populations are shown by the four arrows, with the resonant excitation to the upper level shown by the dark yellow arrow and relaxation to the ground state shown by the violet arrow. Such evolution is equivalently drawn in Fig. 1(a), which behaves like a four-stroke quantum Otto engine [4]. During stage "I", the energy difference ΔE

increases, corresponding to an expansion. The resonant drive during stage "II" increases the upper-level population P_+ as if in contact with a hot thermal reservoir. Then we have the compression during stage "III." Finally, the relaxation during stage "IV" plays the role of contacting with a cold thermal reservoir with decreasing P_+.

An analogous evolution with the resonant excitation in stage "C" is presented in Fig. 1(c), (d). Such a cycle, shown in Fig. 1(c), is reminiscent of a four-stroke refrigerator.

We emphasize that the situation shown in Fig. 1 is for the fast relaxation case $2\pi/\Omega \gg T_{1,2}$. If the modulating frequency Ω is increased, then these two values become comparable, $2\pi/\Omega \sim T_{1,2}$. Then the interference between the different stages can be considered as a superposition of the "heat-engine" and "refrigerator" cycles. In the measured source-drain current, such superposition results in interference fringes, which we present later.

Note that the analogy with a "heat engine" is a partial one. Differences include the lack of high- and low-temperature reservoirs. In our system, the source and the drain are tools to probe the qubit, not heat reservoirs. Namely, the electrodes are reservoirs of electrons and are not directly related to thermal reservoirs. A hot (thermodynamic) reservoir has more energy than a cold (thermodynamic) reservoir. An electronic analog of this would be this: a higher-voltage (electron) reservoir has more energy than a lower-voltage (electron) reservoir.

Slow-modulation regime.—The measured source-drain current I_{SD} is shown in Fig. 2(b) as a function of the driving microwave frequency f_{MW} and the amplitude of the energy-level modulation δf_q for a low-frequency ($\Omega/2\pi = 0.05$ MHz) square modulation, and the phase difference of two modulations $\phi = 90°$. The four lines of the ESR peaks are seen in Fig. 2(b) at such value of ϕ. Next, we vary the phase difference ϕ between the two square-wave modulations, shown in Fig. 3(a). While fixing the two amplitudes of the square modulations to $\delta f_{MW} = \delta f_q$, the phase difference ϕ is changed from 0 to 360°. The heights of the three ESR peaks are changed as in Fig. 3(a). At $\phi = 0$, the height of the center peak is maximum and two side peaks disappear. The condition with $\phi = 0$ and $f_{MW} - f_q = 0$ can be called *in phase*, where the phase of the two modulations matches and the qubit is always in resonance with the microwaves. In contrast, at $\phi = 180°$, the center peak disappears and the heights of two side peaks have their maximum. At this *out-of-phase* condition, $\phi = 180°$ and $f_{MW} - f_q = 0$, the qubit is always driven out of resonance. The height of the center ridge evolves linearly from its maximum (at the in-phase condition) to zero (at the out-of-phase condition) [Fig. 3(a)]. The height simply reflects the duration of the "ON" stage when the microwave is in resonance with the qubit [see Fig. 2(a)].

Fast modulation interference pattern.—Now we increase the modulation frequency up to around T_2^{-1}. Figure 3(b) shows an intensity plot similar to Fig. 3(a), but now the

modulation frequency Ω is set to 2 MHz $\cdot 2\pi$. In Fig. 3(b), there are three vertical ridges, and their positions and heights are similar to the case of the slow modulation. However, there are many fringes in the interference pattern. A ripple-like pattern is seen between the center and side ridges. The edges of the ridges show fan-shaped broadenings, and, importantly, fine periodic interference patterns appear only around the central ridge. Similar to the slow modulation, the central ridge height is maximal at the in-phase condition and zero at the out-of-phase condition. However, due to this interference pattern, the ϕ dependence of the central ridge height shows a "beating" pattern with periodically appearing notches [a cross section is shown in Fig. 3(c)].

We repeat similar measurements with various modulation frequencies, modulation amplitudes, and MW power [36]. For each setting, we repeat similar calibrations as in Fig. 3 and make sure that the condition $\delta f_{\mathrm{MW}} = \delta f_q$ is met. We focus on the period of the notches observed on the central ridge, as indicated in Fig. 3(c), as a characteristic parameter of the interference. The results of calculations are presented in Fig. 3(d)–(f). The period of the notches is proportional to the modulation frequency Ω, i.e., $\Delta\phi/2\pi = \Omega/\delta\omega_{\mathrm{MW}}$, inversely proportional to the modulation amplitude $\delta\omega_q$, i.e., $\Delta\phi/2\pi = \Omega/\delta\omega_q$, and independent of the microwave power G [36].

Conclusion.—We presented a detailed study of an energy- and frequency-modulated two-level system. The experimental realization of this was a spin-qubit device based on a deep impurity in a short-channel silicon TFET. This was shown to work analogously to a heat engine or a refrigerator in the incoherent regime at slow energy-gap modulation, displaying interference fringes in the coherent regime when the modulation period becomes larger than the decoherence time. Note that the coexistence of a classical heat pump and a refrigerator would functionally cancel each other, whereas the quantum superposition of an engine and a cooler exhibits novel interferometric effects. Because of such interference, the quantum thermodynamic system can quickly switch its function between engine or refrigerator regimes and respond quickly to external signals, which is not possible with classical systems. Our impurity-based spin-qubit system has a set of parameters that reliably control its state. This makes it useful for possible applications such as a future universal quantum heat engine.

[*]k-ono@riken.jp
[†]sshevchenko@ilt.kharkov.ua
[‡]fnori@riken.jp

[1] J. Gemmer, M. Michel, and G. Mahler, *Quantum Thermodynamics* (Springer, Berlin Heidelberg New York, 2004).

[2] H. T. Quan, Y.-x. Liu, C. P. Sun, and F. Nori, Quantum thermodynamic cycles and quantum heat engines, Phys. Rev. E **76**, 031105 (2007).

[3] R. Kosloff and A. Levy, Quantum heat engines and refrigerators: Continuous devices, Annu. Rev. Phys. Chem. **65**, 365 (2014).

[4] J. Goold, M. Huber, A. Riera, L. del Rio, and P. Skrzypczyk, The role of quantum information in thermodynamics– A topical review, J. Phys. A **49**, 143001 (2016).

[5] S. Vinjanampathy and J. Anders, Quantum thermodynamics, Contemp. Phys. **57**, 545 (2016).

[6] S. Bhattacharjee and A. Dutta, Quantum thermal machines and batteries, arXiv:2008.07889.

[7] R. Uzdin, A. Levy, and R. Kosloff, Equivalence of Quantum Heat Machines, and Quantum-Thermodynamic Signatures, Phys. Rev. X **5**, 031044 (2015).

[8] J. Klatzow, J. N. Becker, P. M. Ledingham, C. Weinzetl, K. T. Kaczmarek, D. J. Saunders, J. Nunn, I. A. Walmsley, R. Uzdin, and E. Poem, Experimental Demonstration of Quantum Effects in the Operation of Microscopic Heat Engines, Phys. Rev. Lett. **122**, 110601 (2019).

[9] K. Funo, N. Lambert, B. Karimi, J. P. Pekola, Y. Masuyama, and F. Nori, Speeding up a quantum refrigerator via counterdiabatic driving, Phys. Rev. B **100**, 035407 (2019).

[10] D. Gelbwaser-Klimovsky, R. Alicki, and G. Kurizki, Minimal universal quantum heat machine, Phys. Rev. E **87**, 012140 (2013).

[11] P. A. Erdman, V. Cavina, R. Fazio, F. Taddei, and V. Giovannetti, Maximum power and corresponding efficiency for two-level heat engines and refrigerators: Optimality of fast cycles, New J. Phys. **21**, 103049 (2019).

[12] R. Dann, R. Kosloff, and P. Salomon, Quantum finite-time thermodynamics: Insight from a single qubit engine, arXiv:2009.02801.

[13] I. Buluta, S. Ashhab, and F. Nori, Natural and artificial atoms for quantum computation, Rep. Prog. Phys. **74**, 104401 (2011).

[14] T. E. Humphrey, R. Newbury, R. P. Taylor, and H. Linke, Reversible Quantum Brownian Heat Engines for Electrons, Phys. Rev. Lett. **89**, 116801 (2002).

[15] H. T. Quan, Y. D. Wang, Y.-x. Liu, C. P. Sun, and F. Nori, Maxwell's Demon Assisted Thermodynamic Cycle in Superconducting Quantum Circuits, Phys. Rev. Lett. **97**, 180402 (2006).

[16] O. Abah, J. Roßnagel, G. Jacob, S. Deffner, F. Schmidt-Kaler, K. Singer, and E. Lutz, Single-Ion Heat Engine at Maximum Power, Phys. Rev. Lett. **109**, 203006 (2012).

[17] M. Campisi, R. Blattmann, S. Kohler, D. Zueco, and P. Hänggi, Employing circuit QED to measure non-equilibrium work fluctuations, New J. Phys. **15**, 105028 (2013).

[18] M. Campisi, J. Pekola, and R. Fazio, Nonequilibrium fluctuations in quantum heat engines: Theory, example, and possible solid state experiments, New J. Phys. **17**, 035012 (2015).

[19] G. Marchegiani, P. Virtanen, F. Giazotto, and M. Campisi, Self-Oscillating Josephson Quantum Heat Engine, Phys. Rev. Appl. **6**, 054014 (2016).

[20] B. Karimi and J. P. Pekola, Otto refrigerator based on a superconducting qubit: Classical and quantum performance, Phys. Rev. B **94**, 184503 (2016).

[21] P. A. Erdman, F. Mazza, R. Bosisio, G. Benenti, R. Fazio, and F. Taddei, Thermoelectric properties of an interacting quantum dot based heat engine, Phys. Rev. B **95**, 245432 (2017).

[22] M. Josefsson, A. Svilans, A. M. Burke, E. A. Hoffmann, S. Fahlvik, C. Thelander, M. Leijnse, and H. Linke, A quantum-dot heat engine operating close to the thermo-dynamic efficiency limits, Nat. Nanotechnol. **13**, 920 (2018).

[23] J. Roßnagel, S. T. Dawkins, K. N. Tolazzi, O. Abah, E. Lutz, F. Schmidt-Kaler, and K. Singer, A single-atom heat engine, Science **352**, 325 (2016).

[24] G. Maslennikov, S. Ding, R. Hablützel, J. Gan, A. Roulet, S. Nimmrichter, J. Dai, V. Scarani, and D. Matsukevich, Quantum absorption refrigerator with trapped ions, Nat. Commun. **10**, 202 (2019).

[25] D. von Lindenfels, O. Gräb, C. T. Schmiegelow, V. Kaushal, J. Schulz, M. T. Mitchison, J. Goold, F. Schmidt-Kaler, and U. G. Poschinger, Spin Heat Engine Coupled to a Harmonic-Oscillator Flywheel, Phys. Rev. Lett. **123**, 080602 (2019).

[26] M. Grajcar, S. H. W. Van der Ploeg, A. Izmalkov, E. Il'ichev, H.-G. Meyer, A. Fedorov, A. Shnirman, and G. Schön, Sisyphus cooling and amplification by a superconducting qubit, Nat. Phys. **4**, 612 (2008).

[27] F. Nori, Superconducting qubits: Atomic physics with a circuit, Nat. Phys. **4**, 589 (2008).

[28] J. C. Skinner, H. Prance, P. B. Stiffell, and R. J. Prance, Sisyphus Effects in a Microwave-Excited Flux-Qubit Resonator System, Phys. Rev. Lett. **105**, 257002 (2010).

[29] S. N. Shevchenko, D. G. Rubanov, and F. Nori, Delayed-response quantum back action in nanoelectromechanical systems, Phys. Rev. B **91**, 165422 (2015).

[30] M. J. Gullans, J. Stehlik, Y.-Y. Liu, C. Eichler, J. R. Petta, and J. M. Taylor, Sisyphus Thermalization of Photons in a Double Quantum Dot, Phys. Rev. Lett. **117**, 056801 (2016).

[31] S. N. Shevchenko, S. Ashhab, and F. Nori, Landau-Zener-Stückelberg interferometry, Phys. Rep. **492**, 1 (2010).

[32] F. Forster, G. Petersen, S. Manus, P. Hänggi, D. Schuh, W. Wegscheider, S. Kohler, and S. Ludwig, Characterization of Qubit Dephasing by Landau-Zener-Stückelberg-Majorana Interferometry, Phys. Rev. Lett. **112**, 116803 (2014).

[33] K. C. Miao, A. Bourassa, C. P. Anderson, S. J. Whiteley, A. L. Crook, S. L. Bayliss, G. Wolfowicz, G. Thiering, P. Udvarhelyi, V. Ivady, H. Abe, T. Ohshima, A. Gali, and D. D. Awschalom, Electrically driven optical interferometry with spins in silicon carbide, Sci. Adv. **5**, eaay0527 (2019).

[34] R. M. Otxoa, A. Chatterjee, S. N. Shevchenko, S. Barraud, F. Nori, and M. F. Gonzalez-Zalba, A quantum interference capacitor based on double-passage Landau-Zener-Stückelberg-Majorana interferometry, Phys. Rev. B **100**, 205425 (2019).

[35] K. Ono, T. Mori, and S. Moriyama, High-temperature operation of a silicon qubit, Sci. Rep. **9**, 469 (2019).

[36] See Supplemental Material at http://link.aps.org/supplemental/10.1103/PhysRevLett.125.166802 for the details of the device, experiment, and theory.

[37] K. Ono, D. Austing, Y. Tokura, and S. Tarucha, Current rectification by Pauli exclusion in a weakly coupled double quantum dot system, Science **297**, 1313 (2002).

[38] H. W. Liu, T. Fujisawa, Y. Ono, H. Inokawa, A. Fujiwara, K. Takashina, and Y. Hirayama, Pauli-spin-blockade transport through a silicon double quantum dot, Phys. Rev. B **77**, 073310 (2008).

[39] G. Giavaras, N. Lambert, and F. Nori, Electrical current and coupled electron-nuclear spin dynamics in double quantum dots, Phys. Rev. B **87**, 115416 (2013).

[40] K. Ono, G. Giavaras, T. Tanamoto, T. Ohguro, X. Hu, and F. Nori, Hole Spin Resonance and Spin-Orbit Coupling in a Silicon Metal-Oxide-Semiconductor Field-Effect Transistor, Phys. Rev. Lett. **119**, 156802 (2017).

[41] F. H. L. Koppens, C. Buizert, K.-J. Tielrooij, I. T. Vink, K. C. Nowack, T. Meunier, L. P. Kouwenhoven, and L. M. K. Vandersypen, Driven coherent oscillations of a single electron spin in a quantum dot, Nature (London) **442**, 766 (2006).

[42] K. Ono, S. N. Shevchenko, T. Mori, S. Moriyama, and F. Nori, Quantum Interferometry with a g-Factor-Tunable Spin Qubit, Phys. Rev. Lett. **122**, 207703 (2019).

[43] J. Deng, Q.-h. Wang, Z. Liu, P. Hänggi, and J. Gong, Boosting work characteristics and overall heat-engine performance via shortcuts to adiabaticity: Quantum and classical systems, Phys. Rev. E **88**, 062122 (2013).

[44] K. Funo, J.-N. Zhang, C. Chatou, K. Kim, M. Ueda, and A. del Campo, Speeding-Up a Quantum Refrigerator Via Counter-Diabatic Driving, Phys. Rev. Lett. **118**, 100602 (2017).

[45] G. Giavaras and Y. Tokura, Probing the singlet-triplet splitting in double quantum dots: Implications of the ac field amplitude, Phys. Rev. B **100**, 195421 (2019).

[46] S. Savel'ev, F. Marchesoni, P. Hänggi, and F. Nori, Transport via nonlinear signal mixing in ratchet devices, Phys. Rev. E **70**, 066109 (2004).

[47] S. Savel'ev, F. Marchesoni, P. Hänggi, and F. Nori, Non-linear signal mixing in a ratchet device, Europhys. Lett. **67**, 179 (2004).

[48] S. Ooi, S. Savel'ev, M. B. Gaifullin, T. Mochiku, K. Hirata, and F. Nori, Nonlinear Nanodevices Using Magnetic Flux Quanta, Phys. Rev. Lett. **99**, 207003 (2007).

[49] A. M. Satanin, M. V. Denisenko, A. I. Gelman, and F. Nori, Amplitude and phase effects in Josephson qubits driven by a biharmonic electromagnetic field, Phys. Rev. B **90**, 104516 (2014).

[50] M. P. Silveri, J. A. Tuorila, E. V. Thuneberg, and G. S. Paraoanu, Quantum systems under frequency modulation, Rep. Prog. Phys. **80**, 056002 (2017).

[51] S. Mondal, S. Bhattacharjee, and A. Dutta, Exploring the role of asymmetric-pulse modulation in quantum thermal machines and quantum thermometry, Phys. Rev. E **102**, 022140 (2020).

[52] M. P. Silveri, K. S. Kumar, J. Tuorila, J. Li, A. Vepsäläinen, E. V. Thuneberg, and G. S. Paraoanu, Stückelberg interference in a superconducting qubit under periodic latching modulation, New J. Phys. **17**, 043058 (2015).

[53] S. N. Shevchenko, *Mesoscopic Physics Meets Quantum Engineering* (World Scientific, Singapore, 2019).

[54] M. J. Henrich, F. Rempp, and G. Mahler, Quantum thermodynamic Otto machines: A spin-system approach, Eur. Phys. J. Special Topics **151**, 157 (2007).

[55] G. Barontini and M. Paternostro, Ultra-cold single-atom quantum heat engines, New J. Phys. **21**, 063019 (2019).